

ZrO₂-Supported Fe₂O₃ for Chemical-Looping-Based Hydrogen Production: Effect of pH on Its Structure and Performance As Probed by X-ray Absorption Spectroscopy and Electrical Conductivity Measurements

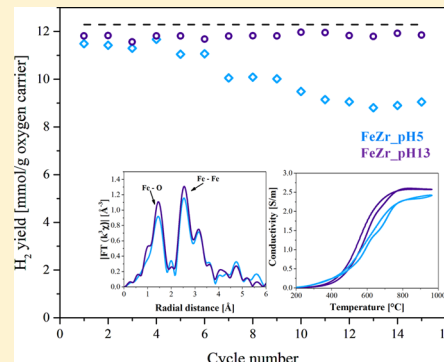
N. Sena Yüzbaşı,[†] Agnieszka M. Kierzkowska,[†] Qasim Imtiaz,[†] Paula M. Abdala,[†] Alexey Kurlov,[†] Jennifer L. M. Rupp,[‡] and Christoph R. Müller*,[†]

[†]Laboratory of Energy Science and Engineering, Department of Mechanical and Process Engineering, ETH Zürich, 8092 Zürich, Switzerland

[‡]Electrochemical Materials, Department of Materials, ETH Zürich, 8093 Zürich, Switzerland

S Supporting Information

ABSTRACT: Chemical looping is a promising process to produce high purity H₂ while simultaneously capturing CO₂. The key requirement for this process is the availability of oxygen carriers that possess a high cyclic redox stability, resistance to carbon deposition, and thermal sintering. In this study, ZrO₂-supported Fe₂O₃-based oxygen carriers were developed using a coprecipitation technique. We assess in detail the influence of the key synthesis parameter, i.e., the pH value at which the precipitation was performed, on the morphological properties, chemical composition, local structure, and cyclic redox stability. The performance of the new oxygen carriers was compared to unsupported Fe₂O₃ and Al₂O₃-supported Fe₂O₃. A higher degree of disorder in the local structure of oxygen carriers precipitated at low pH values was confirmed by X-ray absorption spectroscopy (XAS) measurements. Electrical conductivity measurements showed that supporting Fe₂O₃ on ZrO₂ lowered significantly the activation energy for charge transport when compared to pure Fe₂O₃. In line with this observation, ZrO₂-supported oxygen carriers displayed a very high and stable H₂ yield over 15 redox cycles when precipitation was performed at pH > 5.



1. INTRODUCTION

Hydrogen is a clean energy carrier since its combustion yields only water, and the recent progress in hydrogen powered fuel cell technology has opened up the opportunity to decarbonize the transportation sector.^{1,2} However, for hydrogen to become a promising energy carrier in the future, it must be produced in an efficient and sustainable manner, e.g., from renewable energy sources, such as biomass, or by solar-derived processes. If hydrogen is derived from fossil fuels, the byproduct CO₂ has to be captured and stored.^{3–6}

Steam methane reforming (SMR) followed by a high- and low-temperature water-gas shift reaction is currently the dominating process for the industrial production of hydrogen. However, SMR is a highly endothermic process that requires multiple unit operations to produce high purity hydrogen. Additionally, the SMR releases large quantities of CO₂ into the atmosphere. A further challenge concerning hydrogen is its distribution and transportation. Conventional steam methane reforming plants have large production capacities, i.e., 50 PJ H₂/year.⁷ The scale-down of SMR units, allowing the distributed production of hydrogen on the small and

distributed scale, which is critical if biomass is used as a feedstock, is currently probably prohibitively expensive.^{1,8}

To produce high purity hydrogen from biomass (with the simultaneous capture of CO₂) on a small and distributed scale, a modification of an iron oxide-based chemical looping combustion scheme has been proposed, which was originated from steam–iron process derived by Messerschmitt.⁹ In this process, biomass is first gasified to produce a synthesis gas, i.e., a mixture of predominantly CO and H₂. The synthesis gas is subsequently used to reduce iron oxide to metallic iron, producing thereby a mixture of CO₂ and H₂O. A pure stream of CO₂ is obtained after the condensation of steam. Subsequent reoxidation of metallic iron with steam yields hydrogen of high purity. To close the cycle, the final oxidation step, i.e., from Fe₃O₄ to Fe₂O₃, is performed in air owing to thermodynamic constraints.^{1,8,10–15} A key requirement of the above-described process is the development of iron oxide-based oxygen carriers that possess (i) a high reactivity at typical operation

Received: May 25, 2016

Revised: August 8, 2016

Published: August 8, 2016

temperatures, (ii) cyclic redox stability, and (iii) a high resistance to attrition and synthesis gas impurities. Unsupported iron oxide is not suitable for the above-described process since it deactivates after only a single cycle if reduced completely down to metallic iron, Fe.^{8,10,12,16}

A common attempt to increase the reactivity and cyclability of iron oxide is the addition of a support. The most commonly used supports are alumina (Al_2O_3), magnesium aluminum spinel (MgAl_2O_4), and zirconia (ZrO_2).^{10–12,16–20} For example, Bohn et al.¹ prepared Fe-based oxygen carriers supported on oxides of aluminum, chromium, magnesium, or silicon using wet impregnation (1, 10, or 30 mol % support). Cyclic redox experiments using CO as the reducing gas (850 °C) showed that Fe_2O_3 -supported on Al_2O_3 (10 mol %) gives stable and high yields of hydrogen. Kierzkowska et al.,¹⁰ using a sol–gel technique, prepared several Al_2O_3 -supported oxygen carriers containing different weight ratios of Fe_2O_3 to Al_2O_3 (0.6–0.9). The oxygen carriers containing 60 wt % Fe_2O_3 showed a stable hydrogen production of 7.5 mmol/g for over 40 cycles which is, however, lower than the theoretically expected value of 10.0 mmol/g. Kierzkowska et al.¹⁰ attributed the stability of this particular oxygen carrier to the formation of the spinel structure FeAl_2O_4 (hercynite). The thermodynamically limited reoxidation of FeAl_2O_4 with steam explained the lower than expected hydrogen yield. However, oxidation in air reoxidized FeAl_2O_4 back to Fe_2O_3 and Al_2O_3 . In a further study Imtiaz et al.¹⁸ showed that also MgAl_2O_4 cannot be considered as a fully inert support as the formation of the $\text{MgFe}_{1.4}\text{Al}_{0.6}\text{O}_4$ spinel phase was observed during cyclic redox experiments. On the other hand, ZrO_2 does not seem to form a solid solution with Fe_2O_3 .^{13,21}

Besides the phase stability of the oxygen carriers, also the synthesis parameters can affect strongly the performance of the oxygen carriers. Indeed, previous studies that utilized coprecipitation to synthesize CuO-based oxygen carriers for chemical looping reported that the pH value at which the precipitation reaction was performed influenced strongly the redox performance of the oxygen carriers.^{22,23} Owing to its chemical inertness and very low cationic solubility in the Fe–O–Zr system, ZrO_2 appears to be an attractive support for Fe_2O_3 . However, the influence of the (coprecipitation) synthesis parameters on the morphological and redox characteristics of the oxygen carriers has not been studied in detail for the Fe_2O_3 – ZrO_2 system yet. Thus, the objective of this study is to assess systematically the effect of the pH value at which precipitation is performed on the structural and redox properties for ZrO_2 -stabilized Fe_2O_3 for chemical looping combustion.

2. EXPERIMENTAL SECTION

ZrO_2 -supported, Fe_2O_3 -based oxygen carriers were prepared using coprecipitation. Coprecipitation was performed at four different pH values, i.e., pH 5, pH 7, pH 11, and pH 13, identified from a previously acquired titration curve (Figure S1). Additionally, pure Fe_2O_3 and Al_2O_3 -stabilized Fe_2O_3 were synthesized as reference materials. The following nomenclature is used to describe the oxygen carriers: the symbol Fe is followed by an abbreviation for the support (Zr or Al) and the pH value at which precipitation was performed. For example, FeZr-pH 5 refers to an oxygen carrier that was precipitated at pH 5 and is supported on ZrO_2 . The synthesized oxygen carriers were characterized by X-ray diffraction (XRD), scanning electron microscopy (SEM) equipped with an energy dispersive spectrometer (EDX), N₂ adsorption, attenuated total

reflection Fourier-transformed infrared (ATR-FTIR) spectroscopy, X-ray absorption spectroscopy (XAS), and H₂-temperature-programmed reduction (TPR). The electrical conductivity was determined by four-point conductivity measurements. The cyclic redox stability and H₂ yield were assessed in the fixed bed reactor over 15 cycles at 800 °C. The synthesized oxygen carriers were reduced by CO and reoxidized first by steam, followed by reoxidation in air. Details about the synthesis protocol, material characterization, and cyclic redox tests can be found in the Supporting Information.

3. RESULTS AND DISCUSSION

Morphological and Structural Characterization of the Oxygen Carriers. ATR-FTIR spectroscopy was used to characterize the precipitated compounds. The IR spectra acquired are plotted in Figure S2. The IR spectra show that precipitation with NaOH leads to the formation of hydrous ferric oxides and hydrous zirconium oxides.^{24–28} The hydrous ferric oxide further transformed slowly to goethite ($\alpha\text{-FeOOH}$), at room temperature. The bands located at 882 and 788 cm^{−1} are representative of asymmetric Fe–O–H bending vibrations in goethite.^{26–28} However, peaks due to Fe–O–H vibrations were only observed for oxygen carriers precipitated at pH 13. This was attributed to (i) an increased crystallinity and (ii) the formation of high molecular weight polycations (($\text{Fe}_n(\text{OH})_m^{z+}$) under strongly basic conditions. Indeed, Woude et al.²⁶ reported that peaks due to Fe–O–H vibrations cannot be observed in amorphous precipitates. The broad peak in the range 1280–1520 cm^{−1} is due to asymmetric stretching vibrations of nitrate ions (NO₃[−]). This peak is particularly strong for oxygen carriers precipitated at pH 5 and 7 (when compared to pH 11 and pH 13), indicating the incomplete removal of NO₃[−] during washing for these materials.²⁸

The crystalline phases in the calcined oxygen carriers were determined using X-ray diffraction (XRD). The diffractograms of the calcined oxygen carriers (Figure 1) indicate the presence of hematite (Fe_2O_3) and two polymorphs of zirconium oxide

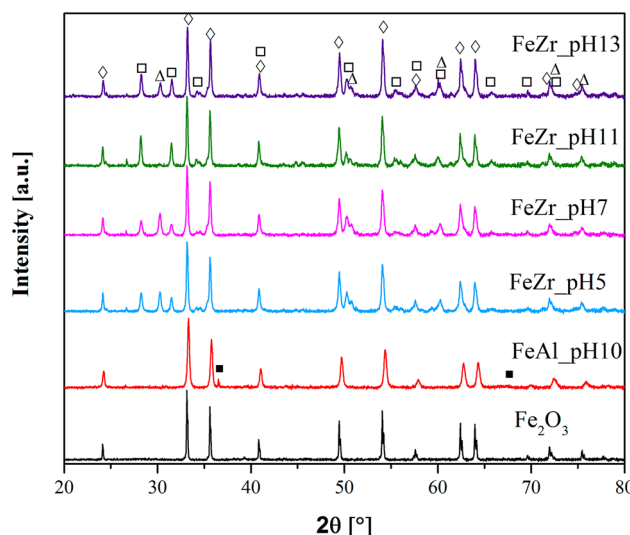


Figure 1. XRD patterns of unsupported Fe_2O_3 , Fe_2O_3 – ZrO_2 precipitated at pH 5, 7, 11, 13, and Fe_2O_3 – Al_2O_3 calcined at 900 °C for 2 h. The following compounds were identified: (◊) hematite, Fe_2O_3 , (□) baddeleyite, m- ZrO_2 , (△) t- ZrO_2 , (■) aluminum oxide, Al_2O_3 .

(ZrO_2), i.e., monoclinic and tetragonal ZrO_2 , independent of the pH value at which precipitation was performed. It is to be noted that monoclinic ZrO_2 is the thermodynamically more stable phase whereas tetragonal ZrO_2 is metastable. The presence of both polymorphs in coprecipitated $\text{FeO}_3\text{--ZrO}_2$ has been reported in previous studies.^{11,29} In the diffractogram of Al_2O_3 -stabilized Fe_2O_3 , weak peaks due to Al_2O_3 were detected. Using the Scherrer equation, the average crystallite size of Fe_2O_3 was determined as ~ 40 nm (Table S1). The crystallite size of Fe_2O_3 did not change significantly with the pH value. It is important to note that the width of a diffraction peak can be affected by inhomogeneous stain and crystal imperfections together with instrumental effects. Therefore, the values calculated for the average crystallite are lower estimates.

To quantify the phases present in the oxygen carriers and to obtain the cell parameters of the different phases, Rietveld refinement was performed on the acquired XRD data (Table S2) of the calcined materials. Rietveld refinement confirms that the quantity of Fe_2O_3 is very similar in the oxygen carriers synthesized, i.e., in the range 70–73 wt %. Nonetheless, we observe an increasing fraction of t- ZrO_2 with decreasing pH values. Furthermore, the tetragonal cell volume in FeZr-pH 5 and FeZr-pH 7 is smaller than in FeZr-pH 13. Importantly, when we compare the unit cell volumes of m- ZrO_2 in the synthesized $\text{Fe}_2\text{O}_3\text{--ZrO}_2$ with pure m- ZrO_2 (synthesized as a reference material), we can conclude that the addition of Fe_2O_3 increases the unit cell volume of m- ZrO_2 (Table S2). Moreover, the unit cell volume of m- ZrO_2 in $\text{Fe}_2\text{O}_3\text{--ZrO}_2$ decreases slightly with decreasing pH value. These observations can be explained by the incorporation of Fe^{3+} cations in the zirconia structure, substituting Zr^{4+} cations. It has been reported that the incorporation of Fe^{3+} in the ZrO_2 lattice stabilizes the metastable t- ZrO_2 phase.^{21,30–33} It should be noted that the mutual cationic solubility in the Fe–O–Zr system is very low, with an equilibrium solubility of Fe_2O_3 in ZrO_2 of 2 mol % and ZrO_2 in Fe_2O_3 of 1 mol % at 1373 K.¹¹

The local structure around Fe in the synthesized oxygen carriers was probed by XAS. Fe K-edge XANES spectra of the calcined oxygen carriers are shown in Figure 2. For comparison, the XANES spectrum of the reference $\alpha\text{-Fe}_2\text{O}_3$ is also provided. The XANES spectrum of the $\alpha\text{-Fe}_2\text{O}_3$ reference shows a main

absorption edge position at ~ 7120 eV (corresponding to the $1s \rightarrow 4p$ electronic transition) and a very intense peak (white line) at ~ 7132 eV. In addition, a pre-edge peak is observed at ~ 7112 eV corresponding to the $1s \rightarrow 3d$ electronic transition. This transition is normally dipole-forbidden in a centrosymmetric site such as a regular octahedron, but it is possible in structures in which the Fe atom is in the symmetrically distorted center.^{34–36} A change in the pre-edge intensity can be an indicator for a distortion around the central atom, e.g., a change in the local oxygen coordination around a Fe atom.³⁵ Qualitatively, all the oxygen carriers synthesized exhibit similar XANES features as $\alpha\text{-Fe}_2\text{O}_3$. This is in agreement with the XRD results. However, the XANES spectra of ZrO_2 -supported Fe_2O_3 exhibit differences in the relative intensities of the characteristic $\alpha\text{-Fe}_2\text{O}_3$ features, such as a lower white line intensity and a higher pre-edge peak intensity. The higher intensity of the pre-edge peak indicates that the octahedral environment of the Fe atom is more distorted in ZrO_2 -supported Fe_2O_3 when compared to (pure) $\alpha\text{-Fe}_2\text{O}_3$. It is worth noting that these differences are more evident for oxygen carriers synthesized at lower pH values.

The Fourier-transformed (FT) EXAFS functions (k^2 -weighted) of the synthesized oxygen carriers (and the reference $\alpha\text{-Fe}_2\text{O}_3$) are shown in Figure S3. In agreement with the XANES and XRD data, all samples exhibit a similar local atomic distribution as the $\alpha\text{-Fe}_2\text{O}_3$ reference. The peaks located in the range 1–2 Å correspond to Fe–O bonds, and those in the range 2–4 Å are dominated by Fe–Fe next-nearest-neighbor distances. In spite of the similarities with the $\alpha\text{-Fe}_2\text{O}_3$ reference, a reduction of the amplitude of the first and second peaks can be observed in the synthesized materials. This observation is indicative of a higher degree of disorder in the local structure of these materials. Quantitative structural information was obtained by nonlinear least-squares fitting of the acquired EXAFS functions. A detailed description of the fitting model is given in the Supporting Information and the structural parameters obtained are reported in Table S3. All experimental EXAFS data could be fitted well using the crystallographic structure of $\alpha\text{-Fe}_2\text{O}_3$, yielding *R*-factors in the range 0.011–0.022. Table S3 shows that larger values for the Debye–Waller factors (σ^2) for Fe–O and Fe–Fe spheres were obtained for ZrO_2 -supported Fe_2O_3 when compared to the $\alpha\text{-Fe}_2\text{O}_3$ reference. In particular, $\text{Fe}_2\text{O}_3\text{--ZrO}_2$ precipitated at lower pH values exhibit higher σ^2 values. The σ^2 value for the second Fe–O sphere decreases in the following order: $\sigma^2_{\text{FeZr-pH 5}} > \sigma^2_{\text{FeZr-pH 7}} > \sigma^2_{\text{FeZr-pH 11}} > \sigma^2_{\text{FeZr-pH 13}} > \sigma^2_{\alpha\text{-Fe}_2\text{O}_3}$. A higher value of σ^2 can be interpreted as a higher disorder in the local environment around a Fe atom. A possible explanation for the increasing disorder and changes in the relative intensity of the pre-edge peak and the white line peak with decreasing pH could be the incorporation of Fe^{3+} into ZrO_2 . However, it is also clear that the majority of Fe is in an $\alpha\text{-Fe}_2\text{O}_3$ type environment since the observed differences between $\text{Fe}_2\text{O}_3\text{--ZrO}_2$ and $\alpha\text{-Fe}_2\text{O}_3$ are relatively small.

We have compared the results of our XAS measurements of ZrO_2 supported Fe_2O_3 to previous literature reports. The shapes of our XANES spectra including pre-edge and post-edge features, the edge positions, and shapes are in close resemblance to $\text{Fe}_2\text{O}_3\text{--ZrO}_2$ systems reported previously.^{32,37,38}

For example, in the study of Yamamoto et al.,³⁸ an increase in the intensity of the pre-edge peak was also attributed to distortions around the local structure of Fe (due to the

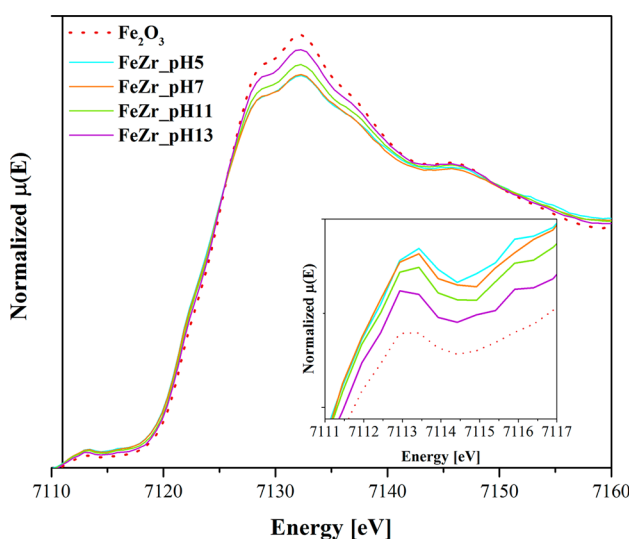


Figure 2. XANES spectra of calcined oxygen carriers.

formation of a solid solution between zirconia and iron oxide). Similarly, Li et al.³² and Ji et al.³⁸ also observed two distinct peaks at 1.6 and 3 Å in the Fourier transformed EXAFS spectra of $\text{Fe}_2\text{O}_3/\text{ZrO}_2$. The first and second peaks were attributed to Fe–O and Fe–Fe scatterers, respectively. However, somewhat contradictory, Mastelaro et al.³⁹ and Yamamoto et al.³⁸ assigned the second peak to Fe–Zr scatters.

The surface morphology of the oxygen carriers was characterized with high-resolution scanning electron microscopy (HR-SEM) and is shown in Figure 3a–d. For comparison,

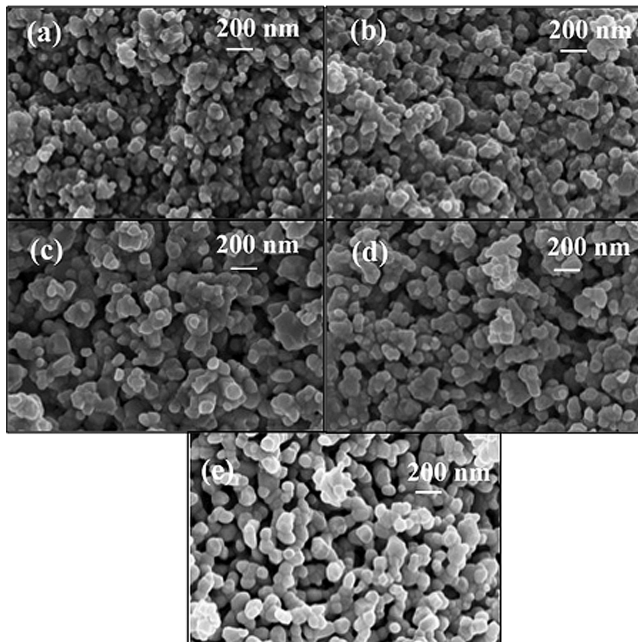


Figure 3. Electron micrographs of the calcined oxygen carriers (a) FeZr-pH 5, (b) FeZr-pH 7, (c) FeZr-pH 11, (d) FeZr-pH 13, and (e) unsupported Fe_2O_3 .

a HR-SEM image of unsupported Fe_2O_3 is given in Figure 3e. The surface of the freshly calcined, unsupported Fe_2O_3 is composed of nanosized grains. The morphology of the freshly calcined ZrO_2 -supported Fe_2O_3 is affected only marginally by the pH value at which the precipitation was performed. Based on the analysis of 20 grains, the average grain size of ZrO_2 -supported Fe_2O_3 was determined as 120 ± 10 nm, independent of the pH at which precipitation was performed.

The BET surface area and BJH pore volume of the calcined oxygen carriers are summarized in Table S1. The measurements show that the pH value at which the precipitation was performed did not influence significantly the surface area and pore volume of the calcined oxygen carriers. The lowest surface area of $4 \text{ m}^2/\text{g}$ was measured for FeZr-pH 5. The oxygen carriers that were precipitated at pH 7, 11, and 13 had slightly larger surface areas, i.e., $7 \text{ m}^2/\text{g}$. Unsupported Fe_2O_3 had a very low surface area of $1 \text{ m}^2/\text{g}$, whereas Al_2O_3 -supported Fe_2O_3 possessed a comparatively high surface area of $19 \text{ m}^2/\text{g}$, which is in agreement with previous studies.^{10,40}

Temperature-Programmed Reduction. The mass fraction of Fe_2O_3 in the calcined oxygen carriers was determined using H_2 -temperature-programmed reduction (TPR), shown in Figure S4. All oxygen carriers were completely reduced during H_2 -TPR. This was confirmed by XRD analysis of the reduced samples. Using the TPR profiles, Fe_2O_3 contents of 73.1, 73.1,

72, and 72.2 wt % were calculated for FeZr-pH 5, FeZr-pH 7, FeZr-pH 11, and FeZr-pH 13, respectively. The iron oxide content determined by H_2 -TPR is substantially higher than the theoretically expected value of 60 wt % Fe_2O_3 , which can be explained by the partial dissolution of Zr^{4+} in aqueous media via $\text{Zr}(\text{OH})_n^{(4-n)+}$ ($n = 1–5$) formation.^{25,41} During washing, soluble polymeric zirconium hydrous oxide species are washed out resulting in an Fe_2O_3 -rich material. The Fe_2O_3 content in FeAl-pH 10 was determined as 77 wt %, in good agreement with the theoretically expected value of 73 wt % Fe_2O_3 .

Figure 4 plots the hydrogen consumption during the TPR experiments as a function of temperature. ZrO_2 -supported

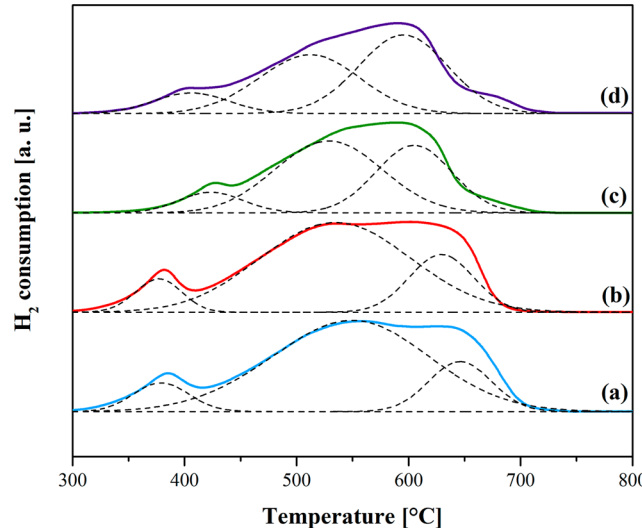


Figure 4. H_2 consumption during TPR of ZrO_2 -stabilized Fe_2O_3 . Precipitation was performed at the following pH values: (a) FeZr-pH 5, (b) FeZr-pH 7, (c) FeZr-pH 11, and (d) FeZr-pH 13.

Fe_2O_3 showed a three-step reduction mechanism, independent of the pH value at which precipitation was performed. During the first, relatively sharp peak located around ~ 350 °C, hematite is reduced to magnetite. For FeZr-pH 11 and FeZr-pH 13, the first reduction step was shifted to higher temperatures, i.e., ~ 400 °C. The reduction peaks for the transitions from magnetite to wüstite and wüstite to metallic iron overlap, leading to a second relatively broad feature in the TPR profile. Deconvolution of the H_2 consumption profiles indicate that the $\text{Fe}_3\text{O}_4 \rightarrow \text{FeO}$ and $\text{FeO} \rightarrow \text{Fe}$ transitions proceed simultaneously and not sequentially. These results are consistent with the work of Galvita et al.,⁴² who reported an (apparent) two-step reduction mechanism from Fe_2O_3 to metallic iron. The peak temperatures of the second and third (fitted) peaks shift to lower temperatures for increasing pH values, indicating a poorer reducibility of FeZr-pH 5 than FeZr-pH 13. The poorer reducibility of FeZr-pH 5 can be attributed to an increased interaction between the oxides of iron and zirconia as confirmed previously by EXAFS modeling (Table S3).

Redox Performance and H_2 Production Capacity of the Synthesized Oxygen Carriers. The redox characteristics of the synthesized oxygen carriers were evaluated over 15 cycles at 800 °C in a fixed bed reactor. For each cycle, the hydrogen yield was calculated according to

$$N_{H_2} = \dot{N}_{N_2} \int \frac{y_{H_2}}{1 - y_{H_2}} dt \quad (1)$$

where N_{H_2} is the number of moles of H_2 produced, \dot{N}_{N_2} is the molar flow rate of N_2 , and y_{H_2} is mole fraction of hydrogen in the gas leaving the fixed bed.

Figure 5 plots the quantity of hydrogen produced, expressed as mmol H_2 /g oxygen carrier, as a function of the cycle number.

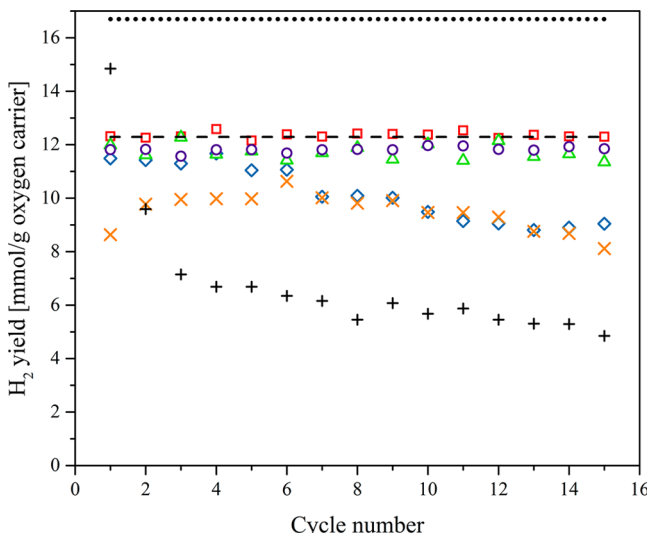


Figure 5. H_2 yield as a function of cycle number: (◊) FeZr-pH 5, (□) FeZr-pH 7, (△) FeZr-pH 11, (○) FeZr-pH 13, (×) FeAl-pH 10, (+) unsupported Fe_2O_3 . The dashed and dotted horizontal lines give the theoretically expected quantities of hydrogen, i.e., 12.3 and 16.7 mmol H_2 /g for oxygen carriers containing 73.6 and 100 wt % Fe_2O_3 , respectively (assuming a full reduction to Fe).

For unsupported iron oxide the hydrogen yield decreased rapidly over 15 cycles, viz. from 13 mmol H_2 /g in the first to only 4.1 mmol H_2 /g in the 15th cycle. The theoretically expected value is 16.7 mmol H_2 /g Fe_2O_3 . The rapidly decreasing hydrogen yield of unsupported Fe_2O_3 has been observed previously by Bohn et al.⁸ and was attributed to severe sintering. Severe sintering and substantial morphological changes of unsupported iron oxide over multiple redox cycles are confirmed by HR-SEM (Figure 6e). Bohn et al.⁸ reported that for unsupported Fe_2O_3 stable H_2 yields could be obtained only when the reduction was limited to FeO . However, since the oxidation of Fe to Fe_3O_4 provides 4 times more hydrogen when compared to the FeO – Fe_3O_4 transition, oxygen carriers that allow the full reduction to Fe are highly desirable.

It is believed that material sintering causes an appreciable decrease in the rate of reduction, leading in turn to incomplete reduction and low H_2 yields during reoxidation. Indeed, the presence of Fe_3O_4 and FeO in the diffractogram of cycled and reduced Fe_2O_3 (Figure S5a) supports this hypothesis. Similarly, the diffractogram of cycled (oxidized), unsupported Fe_2O_3 showed peaks due to Fe_2O_3 , Fe_3O_4 , and FeO indicating that Fe_2O_3 was not reoxidized fully (Figure S5b). Supporting iron oxide on Al_2O_3 resulted in an improved redox performance when compared to unsupported Fe_2O_3 . However, the H_2 yield after 15 cycles (9 mmol H_2 /g) is still substantially below the theoretically expected value of 12.3 mmol H_2 /g. The low H_2 yield is due to the formation of hercynite ($FeAl_2O_4$), as verified by XRD (Figure S5a); the formation of hercynite is

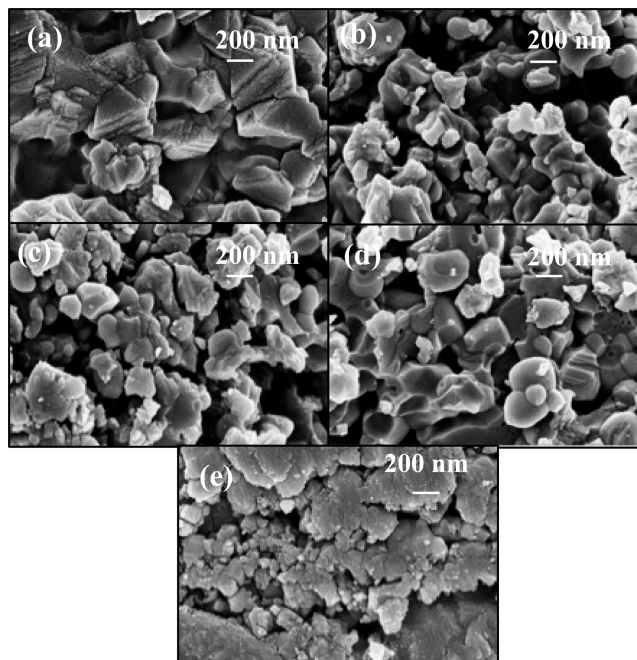


Figure 6. Electron micrographs of oxygen carriers that have undergone 15 redox cycles (oxidized state): (a) FeZr-pH 5, (b) FeZr-pH 7, (c) FeZr-pH 11, (d) FeZr-pH 13, and (e) unsupported Fe_2O_3 .

thermodynamically favored for $8 \times 10^{-2} < P_{CO_2}/P_{CO} < 1.8 \times 10^5$ and $1 \times 10^{-2} < P_{H_2O}/P_{H_2} < 2.1 \times 10^5$ ¹⁰ but undesirable since reoxidation of $FeAl_2O_4$ with steam is thermodynamically limited. In comparison to Al_2O_3 -supported Fe_2O_3 , ZrO_2 -stabilized Fe_2O_3 precipitated at pH 7, 11, or 13 showed very high and stable hydrogen yields close to the theoretically expected value of 12.3 mmol H_2 /g oxygen carrier. The only unstable ZrO_2 -supported Fe_2O_3 is FeZr-pH 5 that starts to deactivate from the sixth cycle onward.

The improved performance of supported Fe_2O_3 (when compared to pure Fe_2O_3) was attributed previously to a higher porosity and an increased sintering resistance, leading to higher surface area materials.⁴³ However, the ZrO_2 -stabilized iron oxide reported here has a very low surface area of $<1\text{ m}^2/\text{g}$ after 15 redox cycles (Table S4). Thus, the high and stable hydrogen yield of ZrO_2 -supported Fe_2O_3 precipitated at pH 7, 11, or 13 cannot be attributed to surface area effects. Instead, we speculate that the redox characteristics of the oxygen carriers are more affected by solid-state ionic diffusion than by intraparticle gaseous diffusion. This hypothesis was also put forward by Li et al.⁴³ and Tan et al.⁴⁴ For example, Li et al.⁴³ probed the oxidation mechanism of unsupported and TiO_2 -supported iron (oxides) using inert marker experiments. It was argued that the transport of oxygen ions through distortions and oxygen vacancies (i.e., ionic diffusivity) rather than porosity is the controlling mechanism during oxidation. These vacancies are formed as a result of substitutional defects that form at the interfaces between iron- and TiO_2 -rich zones in the crystal structure.^{43,45} Using DFT calculations and molecular dynamic simulations, Tan et al.⁴⁴ investigated the influence of ZrO_2 on the electronic structure of Fe_2O_3 and its reaction with CO. The calculations showed that (i) compared to pure Fe_2O_3 , ZrO_2 increased the adsorption energy of CO on Fe_2O_3 from 0.533 to 2.134 eV, promoting in turn the chemisorption of CO on Fe sites, and (ii) the activation energy of the reaction between

chemisorbed CO and lattice oxygen of Fe_2O_3 decreased from 2.59 to 0.826 eV. While these theories can explain the favorable redox performance of FeZr-pH 7, FeZr-pH 11, and FeZr-pH 13, it fails to explain the deactivation of FeZr-pH 5. Therefore, the electrical conduction and charge transport properties of the freshly calcined oxygen carriers were analyzed in more detail using four-point conductivity measurements (Figure 7).

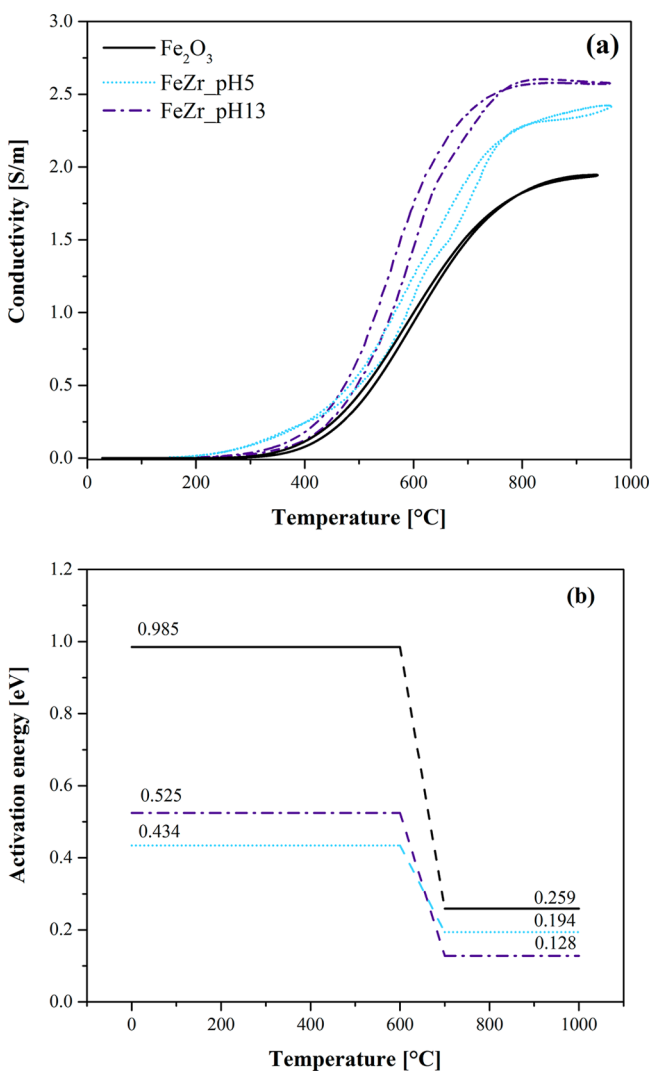


Figure 7. (a) Conductivity as a function of temperature and (b) activation energy for charge transport. The charge transport characteristics of the following oxygen carriers were assessed: (—) Fe_2O_3 , (···) FeZr-pH 5, and (···) FeZr-pH 13.

XRD spectra and energy-dispersive X-ray spectroscopy (EDX) maps of the FeZr-pH 5 and FeZr-13 pellets that were used for the conductivity measurements are presented in Figures S6 and S7, respectively. The XRD spectra confirmed that both of the pellets were composed of Fe_2O_3 and m-ZrO₂. We could not observe the metastable tetragonal zirconia phase in the pellets. Our measurements show that ZrO₂-supported Fe_2O_3 possessed a higher total conductivity when compared to unsupported Fe_2O_3 . The total conductivity increases in the following order $\text{Fe}_2\text{O}_3 < \text{FeZr-pH 5} < \text{FeZr-pH 13}$. The activation energy for charge transport was determined using an Arrhenius relationship (Figure 7b). In Figure 7b, two regions, i.e., a low- and a high-temperature regime (below and above

600 °C, respectively), can be identified. In the high-temperature region, i.e., the region relevant for CLC, the activation energies were 0.259, 0.194, and 0.128 eV for unsupported Fe_2O_3 , FeZr-pH 5, and FeZr-pH 13, respectively (Figure 7). The lower activation energy for charge transport for $\text{Fe}_2\text{O}_3-\text{ZrO}_2$ when compared to unsupported Fe_2O_3 suggests that the presence of ZrO₂ enhances the solid-state diffusion of oxygen anions and electrons in Fe_2O_3 . This is in agreement with the DFT calculations and inert marker experiments of Li et al.⁴³ From Figure 7b, we can also observe that an increasing pH value during precipitation results in a decreasing activation energy for charge transport. We believe that the faster transport of ionic and electronic carriers leads to a higher reduction (and oxidation) rate and, thus, explains the high cyclic oxygen carrying capacity of FeZr-pH 13 when compared to FeZr-pH 5 and Fe_2O_3 .

In order to compare quantitatively the reduction rates of FeZr-pH 5 (deactivating) and FeZr-pH 13 (cyclically stable), the conversion of the oxygen carrier is plotted as a function of time in Figure 8. During a redox cycle the reduction time was

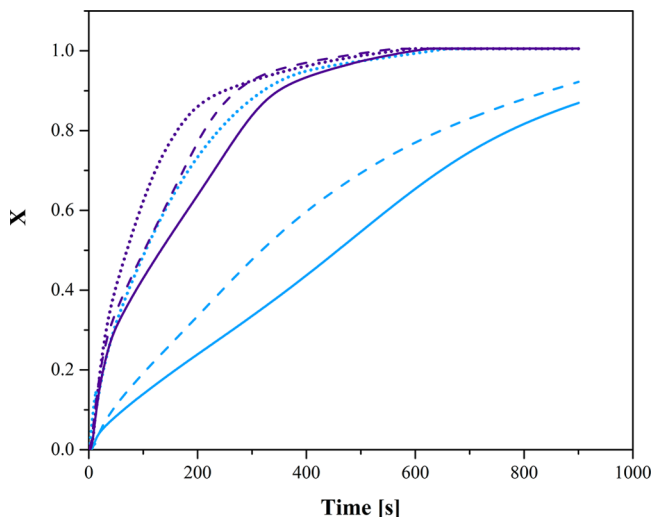


Figure 8. Effect of cycle number [(···) 1st cycle, (- - -) 6th cycle, and ——] on fractional conversion for FeZr-pH 5 (blue) and FeZr-pH 13 (purple).

fixed to 15 min. Already in the first reduction cycle, the conversion of FeZr-pH 5 is appreciably slower than that of FeZr-pH 13, in agreement with the H₂-TPR experiments. With cycle number the apparent reduction rate decreased dramatically for FeZr-pH 5, whereas the overall reduction duration of FeZr-pH 13 is fairly unaffected by the cycle number. Thus, owing to the decreasing reduction rates of FeZr-pH 5 with cycle number, FeZr-pH 5 is not fully reduced within 15 min from cycle number six onward, explaining the decreasing H₂ yields of this material. Furthermore, the diffractograms of the cycled (oxidized) FeZr-pH 5 showed the presence of Fe_2O_3 , Fe_3O_4 , and FeO , indicating that FeZr-pH 5 could not reoxidize fully in the fixed bed reactor due to a decrease in the rate of oxidation (Figure S5b).

To explain in more detail the decreasing reduction kinetics of FeZr-pH 5, energy-dispersive X-ray spectroscopy (EDX) was used to determine the surface composition and the distribution of the different phases in FeZr-pH 5 and FeZr-13 (freshly calcined and after 15 redox cycles, oxidized state). EDX mapping of the freshly calcined oxygen carriers (Figure 9a,b)

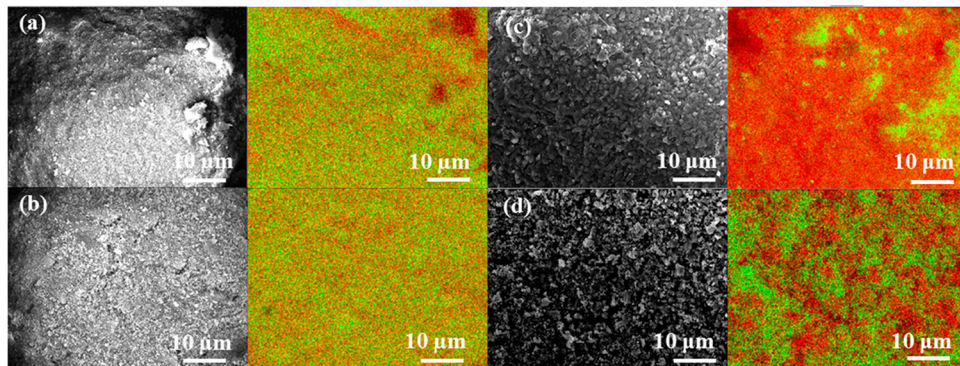


Figure 9. EDX maps of (a) calcined FeZr-pH 5 and (b) calcined FeZr-pH 13 (c) cycled and oxidized FeZr-pH 5 and (d) cycled FeZr-pH 13. The green color represents Zr and the red color Fe.

revealed that in FeZr-pH 13 the two phases Fe_2O_3 and ZrO_2 , were distributed more homogeneously than in FeZr-pH 5. After cycling appreciable difference appeared in the surface composition of FeZr-pH 5 and FeZr-pH 13 in both reduced (Figure S8a,b) and oxidized (Figure 9c,d) states. For FeZr-pH 13, some phase separation occurred; however, Fe_2O_3 and ZrO_2 were still distributed fairly homogeneously. On the other hand, EDX mapping of FeZr-pH 5 revealed a very heterogeneous distribution of the two metal oxides with big clusters of iron oxide and ZrO_2 forming after 15 redox cycles.

The titration curves of pure iron(III) nitrate and zirconium(IV) oxynitrate solutions with NaOH (Figure S9) show that iron and zirconium precursors do not precipitate at the same pH. Thus, it is conceivable that the pH value at which precipitation is performed influences crucially the degree of mixing between the different phases. Indeed, EDX mapping of the freshly calcined oxygen carriers (Figure 9) indicates that the degree of mixing between the iron and zirconium containing phases are affected by the pH, leading in turn to very different conductivity and redox behavior. In addition, the heterogeneous distribution of the Fe_2O_3 and ZrO_2 phases in FeZr-pH 5 affects negatively charge carrier transport. Thus, we attribute the decreasing rate of reduction and redox stability of FeZr-pH 5 to large-scale phase separation.

Purity of Hydrogen. The Boudouard reaction, $2\text{CO} \leftrightarrow \text{CO}_2 + \text{C}_{(\text{s})}$, a side reaction in the proposed process, would lead to CO_x -contaminated hydrogen during reoxidation. Indeed, during steam oxidation CO formation was observed at the start of the reaction, suggesting that some carbon deposition occurred. The average CO contamination of the hydrogen produced, i.e., $[\text{CO}] / ([\text{H}_2] + [\text{CO}])$, for FeZr-pH 5 and FeZr-pH 13, as a function of the duration of the N_2 purge between the reduction and oxidation steps is tabulated in Table 1. Purging with N_2 for 1 min before the oxidation step gave CO levels of <1000 ppm.

Another interesting finding of this study was that after 15 redox cycles for FeZr-pH 5 the CO contamination of hydrogen was notably lower than for FeZr-pH 13. This observation would support the hypothesis that metallic iron catalyzes the Boudouard reaction. For FeZr-pH 13, CO contamination of the hydrogen produced could be avoided completely when the hydrogen yield was limited to 88% (by decreasing the reduction time from 15 to 8 min). A decrease of the reduction time implies an only partial reduction of FeO to metallic iron, thus inhibiting effectively the Boudouard reaction.

Table 1. Carbon Deposition as a Function of Cycle Number, Duration of Reduction, and N_2 Purge

	1 min purging			
	1st cycle		15th cycle	
	CO (ppm)	H_2 yield (%)	CO (ppm)	H_2 yield (%)
FeZr-pH 13	862	97	907	97
FeZr-pH 5	839	95	135	75
30 min purging				
15 min reduction		8 min reduction		
CO (ppm)		H_2 yield (%)	CO (ppm)	H_2 yield (%)
FeZr-pH 13	27	97		88
FeZr-pH 5	32	95	5	88

4. CONCLUSIONS

In this study, we have investigated in detail the effect of the key synthesis parameter (i.e., the pH value) on the morphological properties, phase changes, chemical composition, local structure, and redox characteristics of ZrO_2 -supported Fe_2O_3 . Here, unsupported Fe_2O_3 and $\text{Fe}_2\text{O}_3-\text{Al}_2\text{O}_3$ were used as reference materials. XAS measurements revealed that the static disorder of the local environment around Fe increased with decreasing pH value at which precipitation was performed. Also, the unit cell volume of m-ZrO₂ obtained through Rietveld refinement was smaller for the oxygen carriers precipitated at low pH values when compared to pure m-ZrO₂. These two observations can be explained by the substitution of Zr⁴⁺ by Fe³⁺. H₂-TPR experiments showed that the interaction between the oxides of iron and zirconia influenced the reduction characteristics, leading to a slower rate of reduction for the oxygen carriers that were precipitated at low pH values. Cyclic redox tests demonstrated that unsupported Fe_2O_3 deactivated rapidly when fully reduced to Fe. Supporting iron oxide on Al₂O₃ resulted in an improved redox stability although the H₂ yield was lower than the theoretically expected value due to the formation of unreactive FeAl_2O_4 . On the other hand, zirconia-supported Fe_2O_3 (precipitated at pH 7, 11, and 13) demonstrated excellent redox characteristics, i.e., a very high and stable H₂ yield over 15 redox cycles. Only the oxygen carrier precipitated at pH 5 was found to deactivate with cycle number. The deactivation of FeZr-pH 5 was attributed to a “demixing” of the Fe_2O_3 and ZrO_2 phases with cycle number, thus reducing the materials conductivity and reduction rate.

■ ASSOCIATED CONTENT

§ Supporting Information

The Supporting Information is available free of charge on the ACS Publications website at DOI: [10.1021/acs.jpcc.6b05276](https://doi.org/10.1021/acs.jpcc.6b05276).

Brief explanation of the synthesis protocol and experimental procedure for material characterization and cyclic redox tests; additional structural information and characterization results of the calcined and cycled oxygen carriers ([PDF](#))

■ AUTHOR INFORMATION

Corresponding Author

*E-mail muelchri@ethz.ch, Tel +41 44 632 3440 (C.R.M.).

Notes

The authors declare no competing financial interest.

■ ACKNOWLEDGMENTS

The authors are grateful to the Swiss National Science Foundation (406640_136707) and the Swiss Office of Energy (BFE) for financial support. We also thank Mrs. Lydia Zehnder for her help with the XRD analysis and the Scientific Centre for Optical and Electron Microscopy (ScopeM) for providing training on and access to scanning electron microscopes. We acknowledge SNBL at the ESRF for the provision of beam time and Wouter van Beek for his support during the experimental stage.

■ REFERENCES

- (1) Bohn, C. D.; Cleeton, J. P.; Muller, C. R.; Chuang, S. Y.; Scott, S. A.; Dennis, J. S. Stabilizing Iron Oxide Used in Cycles of Reduction and Oxidation for Hydrogen Production. *Energy Fuels* **2010**, *24*, 4025–4033.
- (2) Shi, Y. U.; Bork, A. H.; Schweiger, S.; Rupp, J. L. M. The Effect of Mechanical Twisting on Oxygen Ionic Transport in Solid-State Energy Conversion Membranes. *Nat. Mater.* **2015**, *14*, 721–727.
- (3) Bork, A. H.; Kubicek, M.; Struzik, M.; Rupp, J. L. M. Perovskite $\text{La}_{0.6}\text{Sr}_{0.4}\text{Cr}_{1-x}\text{CO}_x\text{O}_3$ -Delta Solid Solutions for Solar-Thermochemical Fuel Production: Strategies to Lower the Operation Temperature. *J. Mater. Chem. A* **2015**, *3*, 15546–15557.
- (4) Broda, M.; Kierzkowska, A. M.; Baudouin, D.; Imtiaz, Q.; Coperet, C.; Muller, C. R. Sorbent-Enhanced Methane Reforming over a Ni-Ca-Based, Bifunctional Catalyst Sorbent. *ACS Catal.* **2012**, *2*, 1635–1646.
- (5) Chueh, W. C.; Falter, C.; Abbott, M.; Scipio, D.; Furler, P.; Haile, S. M.; Steinfeld, A. High-Flux Solar-Driven Thermochemical Dissociation of CO_2 and H_2O Using Nonstoichiometric Ceria. *Science* **2010**, *330*, 1797–1801.
- (6) Jarrett, C.; Chueh, W.; Yuan, C.; Kawajiri, Y.; Sandhage, K. H.; Henry, A. Critical Limitations on the Efficiency of Two-Step Thermochemical Cycles. *Sol. Energy* **2016**, *123*, 57–73.
- (7) Hydrogen Production & Distribution, IEA Energy Technology Essentials, 2007; pp 1–4; <http://www.iea.org/publications/freepublications/publication/essentials5.pdf>. Date of access: 06.08.2016.
- (8) Bohn, C. D.; Muller, C. R.; Cleeton, J. P.; Hayhurst, A. N.; Davidson, J. F.; Scott, S. A.; Dennis, J. S. Production of Very Pure Hydrogen with Simultaneous Capture of Carbon Dioxide Using the Redox Reactions of Iron Oxides in Packed Beds. *Ind. Eng. Chem. Res.* **2008**, *47*, 7623–7630.
- (9) Messerschmitt, A. Process of Producing Hydrogen. Google Patents: 1910.
- (10) Kierzkowska, A. M.; Bohn, C. D.; Scott, S. A.; Cleeton, J. P.; Dennis, J. S.; Muller, C. R. Development of Iron Oxide Carriers for Chemical Looping Combustion Using Sol-Gel. *Ind. Eng. Chem. Res.* **2010**, *49*, 5383–5391.
- (11) Liu, W.; Dennis, J. S.; Scott, S. A. The Effect of Addition of ZrO_2 to Fe_2O_3 for Hydrogen Production by Chemical Looping. *Ind. Eng. Chem. Res.* **2012**, *51*, 16597–16609.
- (12) Thursfield, A.; Murugan, A.; Franca, R.; Metcalfe, I. S. Chemical Looping and Oxygen Permeable Ceramic Membranes for Hydrogen Production-a Review. *Energy Environ. Sci.* **2012**, *5*, 7421–7459.
- (13) Keller, M.; Leion, H.; Mattisson, T.; Thunman, H. Investigation of Natural and Synthetic Bed Materials for Their Utilization in Chemical Looping Reforming for Tar Elimination in Biomass-Derived Gasification Gas. *Energy Fuels* **2014**, *28*, 3833–3840.
- (14) Rydén, M.; Arjmand, M. Continuous Hydrogen Production via the Steam–Iron Reaction by Chemical Looping in a Circulating Fluidized-Bed Reactor. *Int. J. Hydrogen Energy* **2012**, *37*, 4843–4854.
- (15) Mei, D.; Abad, A.; Zhao, H.; Adámez, J.; Zheng, C. On a Highly Reactive $\text{Fe}_2\text{O}_3/\text{Al}_2\text{O}_3$ Oxygen Carrier for in Situ Gasification Chemical Looping Combustion. *Energy Fuels* **2014**, *28*, 7043–7052.
- (16) Adámez, J.; Abad, A.; García-Labiano, F.; Gayán, P.; de Diego, L. F. Progress in Chemical-Looping Combustion and Reforming Technologies. *Prog. Energy Combust. Sci.* **2012**, *38*, 215–282.
- (17) Galvita, V.; Sundmacher, K. Cyclic Water Gas Shift Reactor (CWGS) for Carbon Monoxide Removal from Hydrogen Feed Gas for PEM Fuel Cells. *Chem. Eng. J.* **2007**, *134*, 168–174.
- (18) Imtiaz, Q.; Yuzbasi, N. S.; Abdala, P. M.; Kierzkowska, A. M.; van Beek, W.; Broda, M.; Muller, C. R. Development of MgAl_2O_4 -Stabilized, Cu-Doped, Fe_2O_3 -Based Oxygen Carriers for Thermochemical Water-Splitting. *J. Mater. Chem. A* **2016**, *4*, 113–123.
- (19) Otsuka, K.; Kaburagi, T.; Yamada, C.; Takenaka, S. Chemical Storage of Hydrogen by Modified Iron Oxides. *J. Power Sources* **2003**, *122*, 111–121.
- (20) Takenaka, S.; Kaburagi, T.; Yamada, C.; Nomura, K.; Otsuka, K. Storage and Supply of Hydrogen by Means of the Redox of the Iron Oxides Modified with Mo and Rh Species. *J. Catal.* **2004**, *228*, 66–74.
- (21) Saha, S.; Nandy, A.; Meikap, A. K.; Pradhan, S. K. Microstructure Characterization and Electrical Transport Properties of Nanocrystalline Fe and Fe-Doped Cubic Zirconia Cermets Synthesized by Mechanical Alloying. *Mater. Res. Bull.* **2015**, *68*, 66–74.
- (22) Chuang, S. Y.; Dennis, J. S.; Hayhurst, A. N.; Scott, S. A. Development and Performance of Cu-Based Oxygen Carriers for Chemical-Looping Combustion. *Combust. Flame* **2008**, *154*, 109–121.
- (23) Imtiaz, Q.; Kierzkowska, A. M.; Muller, C. R. Coprecipitated, Copper-Based, Alumina-Stabilized Materials for Carbon Dioxide Capture by Chemical Looping Combustion. *ChemSusChem* **2012**, *5*, 1610–1618.
- (24) Guo, G. Y.; Chen, Y. L.; Ying, W. J. Thermal, Spectroscopic and X-Ray Diffraction Analyses of Zirconium Hydroxides Precipitated at Low pH Values. *Mater. Chem. Phys.* **2004**, *84*, 308–314.
- (25) Kobayashi, T.; Sasaki, T.; Takagi, I.; Moriyama, H. Solubility of Zirconium(IV) Hydrous Oxides. *J. Nucl. Sci. Technol.* **2007**, *44*, 90–94.
- (26) Van Der Woude, J. H. A.; De Bruyn, P. L. Formation of Colloidal Dispersions from Supersaturated Iron(Iii) Nitrate Solutions. I. Precipitation of Amorphous Iron Hydroxide. *Colloids Surf.* **1983**, *8*, 55–78.
- (27) Wang, X. F.; Andrews, L. Infrared Spectra of $\text{M}(\text{OH})(1,2,3)$ ($\text{M} = \text{Mn}, \text{Fe}, \text{Co}, \text{Ni}$) Molecules in Solid Argon and the Character of First Row Transition Metal Hydroxide Bonding. *J. Phys. Chem. A* **2006**, *110*, 10035–10045.
- (28) Zic, M.; Ristic, M.; Music, S. Monitoring the Hydrothermal Precipitation of $\alpha\text{-Fe}_2\text{O}_3$ from Concentrated $\text{Fe}(\text{NO}_3)_3$ Solutions Partially Neutralized with NaOH. *J. Mol. Struct.* **2011**, *993*, 115–119.
- (29) Basahel, S. N.; Ali, T. T.; Narasimharao, K.; Bagabas, A. A.; Mokhtar, M. Effect of Iron Oxide Loading on the Phase Transformation and Physicochemical Properties of Nanosized Mesoporous ZrO_2 . *Mater. Res. Bull.* **2012**, *47*, 3463–3472.
- (30) Boukamp, B. A.; Raming, T. P.; Winnubst, A. J. A.; Verweij, H. Electrochemical Characterisation of 3Y-TZP- Fe_2O_3 Composites. *Solid State Ionics* **2003**, *158*, 381–394.
- (31) Lamperti, A.; Cianci, E.; Ciprian, R.; Sangalli, D.; Debernardi, A. Stabilization of Tetragonal/Cubic Phase in Fe Doped Zirconia Grown by Atomic Layer Deposition. *Thin Solid Films* **2013**, *533*, 83–87.

- (32) Li, P.; Chen, I. W.; Penner-Hahn, J. E. Effect of Dopants on Zirconia Stabilization—an X-Ray Absorption Study: I, Trivalent Dopants. *J. Am. Ceram. Soc.* **1994**, *77*, 118–128.
- (33) Popović, S.; Grzeta, B.; Czakó-Nagy, I.; Musić, S. Structural Properties of the Systemm-ZrO₂-α-Fe₂O₃. *J. Alloys Compd.* **1996**, *241*, 10–15.
- (34) de Smit, E.; Beale, A. M.; Nikitenko, S.; Weckhuysen, B. M. Local and Long Range Order in Promoted Iron-Based Fischer-Tropsch Catalysts: A Combined in-situ X-Ray Absorption Spectroscopy/Wide Angle X-Ray. *J. Catal.* **2009**, *262*, 244–256.
- (35) Holzapfel, M.; Proux, O.; Strobel, P.; Darie, C.; Borowski, M.; Morcrette, M. Effect of Iron on Delithiation in Li_xCo_{1-y}Fe_yO₂. Part 2: In-Situ Xanes and Exafs Upon Electrochemical Cycling. *J. Mater. Chem.* **2004**, *14*, 102–110.
- (36) Moog, I.; Feral-Martin, C.; Duttine, M.; Wattiaux, A.; Prestipino, C.; Figueroa, S.; Majimel, J.; Demouragues, A. Local Organization of Fe³⁺ into Nano-CeO₂ with Controlled Morphologies and Its Impact on Reducibility Properties. *J. Mater. Chem. A* **2014**, *2*, 20402–20414.
- (37) Ji, W.; Kuo, Y.; Shen, S.; Li, S.; Wang, H. Xanes, Exafs and Reaction Studies of Some Well-Dispersed Ferric Oxide Catalysts. *Stud. Surf. Sci. Catal.* **1993**, *75*, 2059–2062.
- (38) Yamamoto, T.; Tanaka, T.; Takenaka, S.; Yoshida, S.; Onari, T.; Takahashi, Y.; Kosaka, T.; Hasegawa, S.; Kudo, M. Structural Analysis of Iron and Manganese Species in Iron-and Manganese-Promoted Sulfated Zirconia. *J. Phys. Chem. B* **1999**, *103*, 2385–2393.
- (39) Mastelaro, V. R.; Bríois, V.; de Souza, D. P.; Silva, C. L. Structural Studies of a ZrO₂–CeO₂ Doped System. *J. Eur. Ceram. Soc.* **2003**, *23*, 273–282.
- (40) Kidambi, P. R.; Cleeton, J. P.; Scott, S. A.; Dennis, J. S.; Bohn, C. D. Interaction of Iron Oxide with Alumina in a Composite Oxygen Carrier During the Production of Hydrogen by Chemical Looping. *Energy Fuels* **2011**, *26*, 603–617.
- (41) Veyland, A.; Dupont, L.; Pierrard, J.-C.; Rimbault, J.; Aplincourt, M. Thermodynamic Stability of Zirconium (IV) Complexes with Hydroxy Ions. *Eur. J. Inorg. Chem.* **1998**, *1998*, 1765–1770.
- (42) Galvita, V.; Sundmacher, K. Redox Behavior and Reduction Mechanism of Fe₂O₃–CeZrO₂ as Oxygen Storage Material. *J. Mater. Sci.* **2007**, *42*, 9300–9307.
- (43) Li, F.; Sun, Z.; Luo, S.; Fan, L.-S. Ionic Diffusion in the Oxidation of Iron—Effect of Support and Its Implications to Chemical Looping Applications. *Energy Environ. Sci.* **2011**, *4*, 876–880.
- (44) Tan, Q.; Qin, W.; Chen, Q.; Dong, C.; Li, W.; Yang, Y. Synergistic Effect of ZrO₂ on the Oxidation–Reduction Reaction of Fe₂O₃ During Chemical Looping Combustion. *Appl. Surf. Sci.* **2012**, *258*, 10022–10027.
- (45) Qin, L.; Cheng, Z.; Fan, J. A.; Kopechek, D.; Xu, D.; Deshpande, N.; Fan, L.-S. Nanostructure Formation Mechanism and Ion Diffusion in Iron–Titanium Composite Materials with Chemical Looping Redox Reactions. *J. Mater. Chem. A* **2015**, *3*, 11302–11312.